

Article

Co-Seismic and Postseismic Fault Models of the 2018 Mw 6.4 Hualien Earthquake Occurred in the Junction of Collision and Subduction Boundaries Offshore Eastern Taiwan

Ying-Hui Yang ¹, Jyr-Ching Hu ^{2,*}, Hsin Tung ² , Min-Chien Tsai ³, Qiang Chen ⁴, Qian Xu ⁴, Yi-Jun Zhang ⁴, Jing-Jing Zhao ⁴, Guo-Xiang Liu ⁴, Jun-Nan Xiong ¹ , Ji-Yan Wang ¹, Bing Yu ¹, Chun-Ying Chiu ² and Zhe Su ⁵

¹ School of Civil Engineering and Architecture, Southwest Petroleum University, Chengdu 610500, China; xzhfhyyy@126.com (Y.-H.Y.); neu_xjn@163.com (J.-N.X.); wangjiyan@swpu.edu.cn (J.-Y.W.); rs_insar_bingyu@163.com (B.Y.)

² Department of Geosciences, National Taiwan University, Taipei 10617, Taiwan; cuzn0517@gmail.com (H.T.); aquarous@gmail.com (C.-Y.C.)

³ Seismological Center, Central Weather Bureau, Taipei 10048, Taiwan; minchyen@cwb.gov.tw

⁴ Department of Remote Sensing and Geoinformation Engineering, Southwest Jiaotong University, Chengdu 610031, China; swjtucq@sina.com (Q.C.); 15902837201@163.com (Q.X.); 15108377534@163.com (Y.-J.Z.); zhaojingjing_swjtu@163.com (J.-J.Z.); rsgxliu@swjtu.edu.cn (G.-X.L.)

⁵ Key Laboratory of Crustal Dynamics, Institute of Crustal Dynamics, China Earthquake Administration, Beijing 100036, China; szhe1230@126.com

* Correspondence: jchu@ntu.edu.tw; Tel.: +886-092-227-3830

Received: 7 August 2018; Accepted: 28 August 2018; Published: 29 August 2018



Abstract: The ascending and descending InSAR deformations derived from ALOS-2 and Sentinel-1 satellite SAR images and GPS displacements are used to estimate the fault model of the 2018 Mw 6.4 Hualien earthquake. The sinistral strike-slip fault dipping to the west with a high dip angle of 89.4° and a rake angle of 201.7° is considered as the seismogenic fault of this event. This seismogenic fault also triggered the ruptures of the Milun fault, which dips to the east with a dip angle of ~72°, and an unknown west-dipping fault with a dip angle of 85.2°. Two predicted faulting models indicate that the InSAR deformation fields include more postseismic slip than those of the GPS data. The north segment of the Milun fault and west-dipping fault have been triggered by the rupture of the seismogenic fault, but the postseismic slip occurred only in the south segment of the Milun fault. The InSAR-derived co-seismic and postseismic faulting model suggests that the significant slip concentrates at depths of 2.4–15.0 km of the main fault, 0.0–14.0 km of the Milun fault. Only minor slip is detected on the west-dipping fault. The maximum fault slip of ca. 2.1 m is located at the depth of ca. 2.4 km under the Meilun Tableland. The Coulomb failure stress (CFS) change calculated by the co-seismic and postseismic faulting model shows that there is a significant CFS increase in the east of the south segment of the Milun fault, but few of the aftershocks occur in this area, which indicates a high risk of future seismic hazard.

Keywords: Hualien earthquake; InSAR; co-seismic and post-seismic faulting model; triggered fault; Coulomb failure stress change

1. Introduction

On 6 February 2018, a Mw 6.4 earthquake struck East Taiwan, and the epicenter (24.134°N and 121.658°E, USGS solution) is located at ca. 18.2 km NNE of Hualien City (Figure 1). This strong

earthquake caused the collapse of some buildings in Hualien City, and resulted in 17 deaths and 285 injuries as of 12 February 2018. This earthquake occurred in the northern extension of the Coastal Range which is the junction of collision and subduction boundaries between the Eurasian plate and the Philippine Sea plate. Previous studies suggested that a tear fault boundary could be the major seismogenic structure between the Taiwan orogen and Ryukyu subduction zone [1–3]. The GPS measurements in this area show that the Philippine Sea plate has a movement along NW direction at a rate of ca. 8.2 cm/year towards the Eurasian plate [4]. The high rate of the collision between the two plates causes a very rapid uplift and develops a series of active faults in the east Coastal Range of Taiwan. It also results in many destructive earthquakes, including the 1951 Hualien-Taitung earthquake sequences, the 1999 Mw 7.6 Chi-Chi earthquake, and the 2016 Mw 6.5 Meinong earthquake occurred in Taiwan in the past 100 years [5–8].

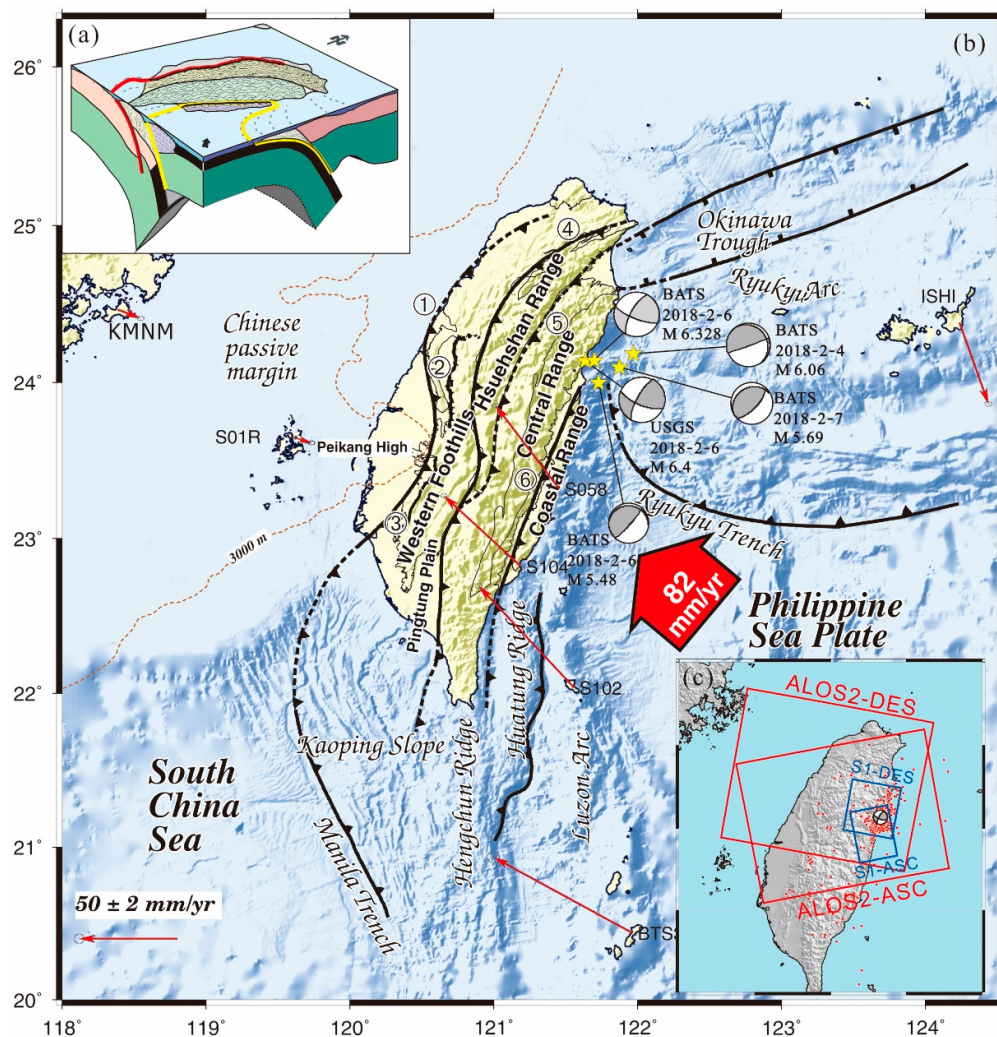


Figure 1. (a) Tectonic setting of Taiwan characterized by opposing subduction systems in the north and south [9]. (b) Main fault systems (the black lines) of Taiwan orogeny. Seven GPS sites (red arrows) located at the Eurasia and Philippine Sea plates are got from the previous study [10], which show a NW directed block motion with an average velocity of ca. 8.2 cm/year [10]. The yellow star indicates the epicenter of the 2018 Hualien earthquake, and the beach balls are the focal mechanisms of the main shocks and major aftershocks of the 2018 Hualien events solved by USGS and BATS based on the New Automatic Full-Waveform Regional Moment Tensor Inversion Algorithm [11]. (c) SAR coverages (the red and blue lines) and aftershocks (red circles) are mapped on the digital Earth model with a high resolution of 30 m.

Previous studies suggest frequent strong seismic activities in the east Coastal Range of Taiwan [12,13], especially along the Longitudinal Valley fault [14]. However, only one historical big event (the 1951 M_L 7.3 Hualien-Taitung earthquake) has been reported that occurred around the Hualien area and resulted in the rupture of the Milun fault [15,16]. The 2018 Mw 6.4 Hualien earthquake is the earthquake with the largest magnitude occurring in the Hualien area in the past ca. 70 years, and it triggered the Milun fault again. The focal mechanism derived from teleseismic data by USGS shows that the co-seismic fault of the 2018 Hualien event has a strike angle of 209° and dips to the west with a high dip angle of 73°. BATS gives a nodal plane of strike angle of 111.5°, dipping to the west with a dip angle of 74.2° and a slip of 157.3°. It suggests that the Milun fault (dipping to east) is not the seismogenic fault of the Hualien event and, thus, it should be triggered by the motion of the seismogenic fault. Therefore, the 2018 Hualien earthquake should be a multi-fault rupture like the 2016 Mw 7.8 Kaikōura earthquake that occurred in New Zealand [17].

A complex multi-fault motion, including the seismogenic fault and Milun fault rupture, should be responsible for the 2018 Hualien earthquake. However, the multi-fault geometry parameters, slip distribution, and the Coulomb failure stress (CFS) transmission from the seismogenic fault to the triggered fault are not well known so far. Here, we firstly map the seismic surface deformation fields using the ALOS-2 and Sentinel-1 synthetic aperture radar (SAR) images and the GPS observations. The ascending and descending InSAR data are used to infer the fault geometry model of the 2018 Hualien event. Then, The GPS and InSAR are respectively used to infer the co-seismic and the co-seismic and postseismic slip models of this event. We calculate the CFS change of both the triggered Milun and west-dipping faults due to the motion of the seismogenic fault. Finally, we investigate the CFS change with varying receiver parameters at the average depth of the aftershocks.

2. Materials and Methods

2.1. Data and Interpretation

We collect the ascending and descending SAR images before and after the main quake acquired by ALOS-2 and Sentinel-1 satellites. Table 1 shows the main information of the used ALOS-2 and Sentinel-1 SAR images. The red (ALOS-2) and blue (Sentinel-1) solid rectangles in Figure 1 show the coverage of the four tracks, and it is obvious that all of them cover the main seismic zone.

Table 1. Parameters of interferometric pairs of ALOS-2 and Sentinel-1 SAR images.

Sensor	Orbital Path	Acquisition Time (M-D-Y)	Heading Angle t(°)	Incidence Angle (°)	B _⊥ (m)
ALOS-2	Ascending	Master: 11-05-2016 Slave: 02-10-2018	349.0	27.8	-159.8
ALOS-2	Descending	Master: 06-18-2017 Slave: 02-11-2018	190.3	40.5	224.0
Sentinel-1	Ascending	Master: 02-03-2018 Slave: 02-09-2018	347.6	39.4	-9.2
Sentinel-1	Descending	Master: 02-05-2018 Slave: 02-11-2018	192.4	33.9	-42.9

We process both the ascending and descending ALOS-2 PALSAR images using the GAMMA software [18]. The multilook factor is set as 18 (azimuth multilook factor) × 8 (range multilook factor) to maintain a high interferometric coherence. The topographic phase component is calculated based on the orbital data and the SRTM-4 digital elevation model [19], and is then removed from the original InSAR interferograms. The 2-D ramp is estimated based on the far-field high-coherence unwrapped phase data, to remove the orbital error from the original InSAR observations [20]. The ascending and descending Sentinel-1 SAR data are processed using the ISCE (InSAR Scientific Computing Environment) software [21].

Figure 2a,c shows that both the ascending and descending ALOS-2 InSAR maintain a reliable interferometric coherence in the main seismic zone. It should be noted that the descending ALOS-2 does not cover the area of the south of the west-dipping fault, and minor surface deformation has been detected by the ALOS-2 ascending InSAR data in this area. Figure 2e,g are the Sentinel-1 ascending and descending InSAR deformation fields of the 2018 Hualien event. It is obvious that the fringes in Sentinel-1 interferograms are similar to the results of ALOS-2, which is due to the two satellites sharing the approximate flight azimuth angles and radar incidence angles (Table 1). It can be seen from Figure 2e,g that both the ascending and descending Sentinel-1 InSAR interferograms lose the interferometric coherence in the area near the Milun and the west-dipping fault, which is attributed to the large deformation gradient and short radar wavelength of 5.5 cm. All the InSAR interferograms show interferometric decorrelation in the west of the main seismic zone, which should result from the dense vegetation covering in the Central Range of Taiwan.

Figure 2b,d,f and h show the absolute InSAR deformation fields of the 2018 Hualien event. It should be noted that both the positive and negative InSAR deformations have been simultaneously detected in the hanging wall along the strike direction of the seismogenic fault (ALOS-2 and Sentinel-1 ascending tracks). It suggests that the measured InSAR deformation should be resulted from a predominant strike-slip event. Moreover, the significant surface deformation is found in the east of the Milun fault, which indicates that this fault should have been triggered by the motion of the seismogenic fault. In addition, the interferometric decorrelation is found in the east of the west-dipping fault, which could be attributed to the shallow fault patch rupture of the west-dipping fault and/or the vegetation cover in this area.

The surface displacements of the 2018 Hualien earthquake have also been observed by the GPS sites around the seismic zone. We remove several sites closing to the triggered shallow folds that weren't modeled, moreover, the far-field sites with abnormal displacements are also not used in this study. The Figure 3 shows the displacements of the remaining 25 GPS sites. The significant horizontal and vertical displacements are found around the Milun and west-dipping fault, which suggests that both of them may rupture in the 2018 Hualien earthquake.

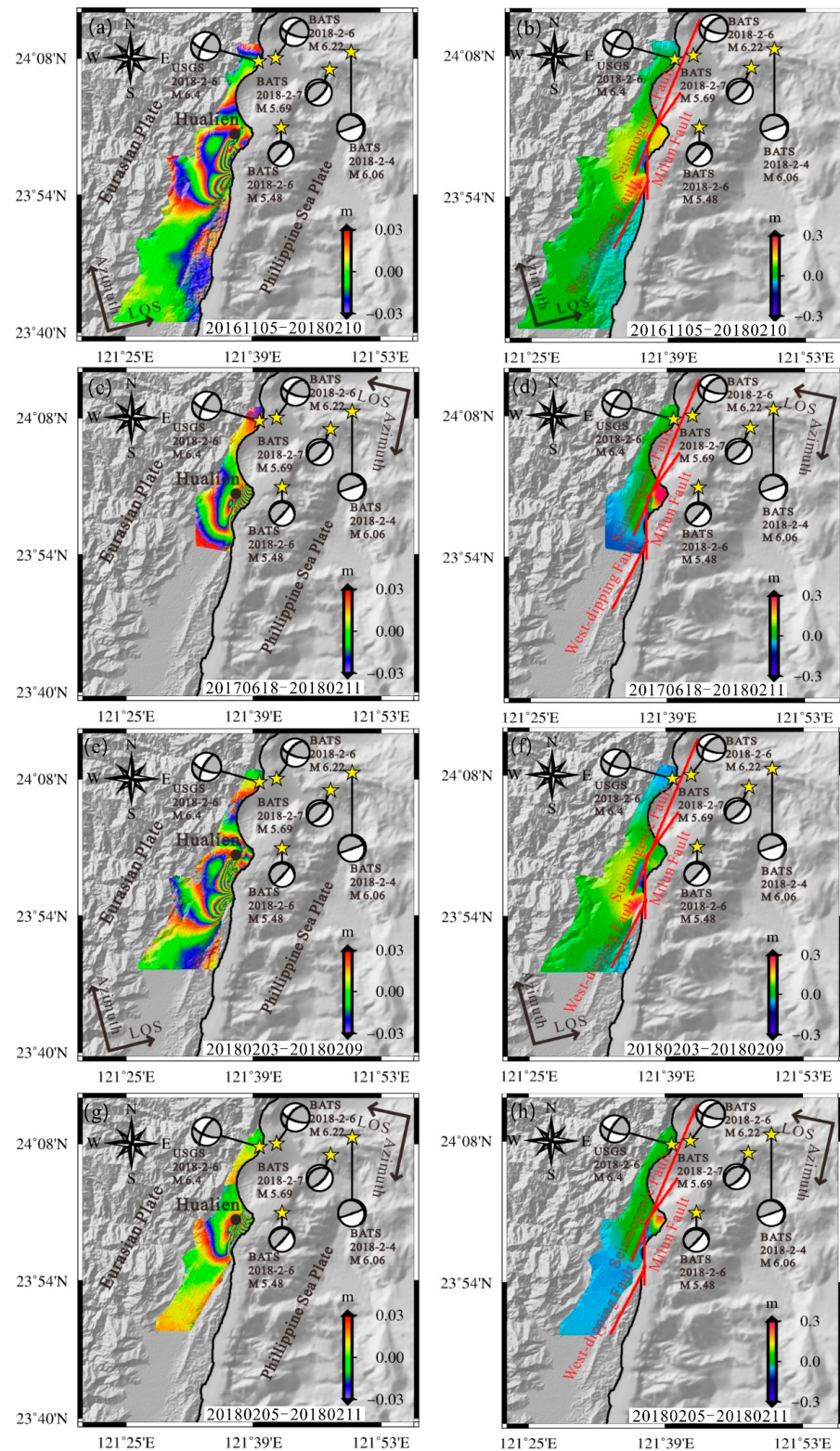


Figure 2. Mapped surface deformation fields of the 2018 Hualien earthquake using the ALOS-2 and Sentinel-1 SAR images. **(a)** ALOS-2 ascending, **(c)** ALOS-2 descending, **(e)** Sentinel-1 ascending, and **(g)** Sentinel-1 descending InSAR deformation is wrapped by $[-3.0 \text{ cm}, 3.0 \text{ cm}]$. **(b)**, **(d)**, **(f)** and **(h)** are the absolute InSAR deformation fields of the 2018 Hualien earthquake. The yellow star indicates the epicenter of the 2018 Hualien earthquakes and major aftershocks, and the beach balls are the focal mechanisms of the main shocks and major aftershocks of the 2018 Hualien events solved by USGS and BATS.

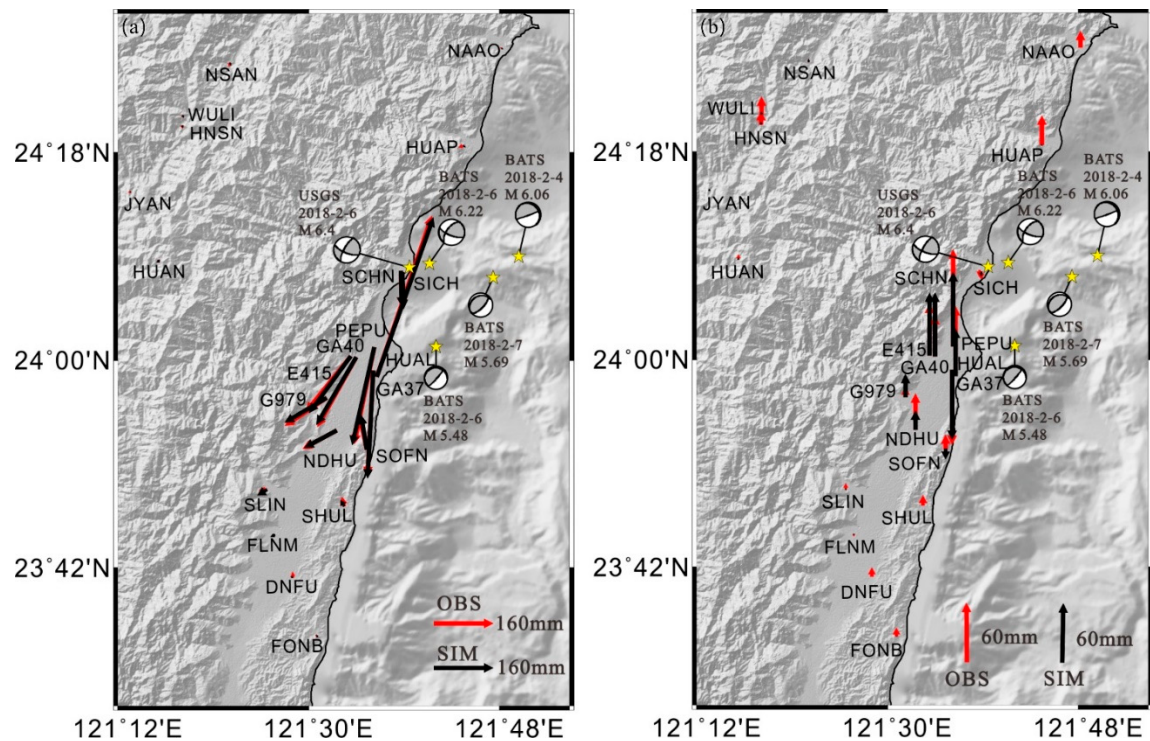


Figure 3. The co-seismic GPS displacements of the 2018 Hualien earthquakes. (a) The GPS horizontal surface displacements in the seismic zone of the 2018 Hualien event. The red vectors are the observed GPS displacements, the black vectors are the predicted GPS displacements based on the co-seismic faulting model shown in Figure 4a, and the beach balls are the focal mechanisms of the main shocks and major aftershocks of the 2018 Hualien events solved by USGS and BATS. (b) The observed (red vectors) and predicted (black vectors) GPS vertical displacements.

2.2. Modeling Estimated by Geodetic Data

First, we must point out that the GPS and InSAR observations are incompatible in the joint inversion of this earthquake. It is believed that such incompatibility results from the fact that more postseismic deformations are included in the InSAR observations than the GPS data, considering that the InSAR observations are contributed by the co-seismic and postseismic slip during the span of the satellite revisiting, but the GPS displacements mostly result from the co-seismic slip. Furthermore, the dense multi-sight InSAR deformations can provide sufficient constraints on the fault geometry and slip parameters of the earthquake [22]. Therefore, only the four tracks of InSAR observations are used to estimate the fault geometry model of the 2018 Hualien earthquake.

To avoid the negative effect on the estimated faulting model by unreliable InSAR observations, a coherence threshold of 0.3 has been used to remove the observations with low coherence. Then, the remained high-coherence data is down-sampled using the two dimensional quadtree algorithm [23]. We totally preserve 2674 ALOS-2 data and 2458 Sentinel-1 data over the entire seismic zone of the Hualien earthquake, and they will be used to infer both the co-seismic fault geometry parameters and the slip distribution of the Hualien event.

We carry out the geodetic modeling of the Hualien earthquake using the proposed method by Yang et al. in 2018. First, we construct the initial fault model composed by the seismogenic fault dipping to the west, the Milun fault dipping to the east and the west-dipping fault dipping to the west to describe the co-seismic fault of the 2018 Hualien event. Then, we set the bounds of $[180^\circ, 240^\circ]$ for the strike angle, $[0^\circ, 90^\circ]$ for the dip angle, $[-90^\circ, 90^\circ]$ for the rake angle, and $[-20 \text{ km}, 0 \text{ km}]$ for the depth of the seismogenic fault based on the USGS solution. The Milun fault is divided into three segments based on the InSAR deformations and field investigation. We set the bounds of $[-10^\circ, 10^\circ]$

for the strike angle and $[0^\circ, 90^\circ]$ for the dip angle of the south segment, and $[30^\circ, 50^\circ]$ for the strike angle and $[0^\circ, 90^\circ]$ for the dip angle of the north segment. The depth of the Milun fault is set as zero due to the significant surface rupture trace along the Milun fault found in the field investigation. Furthermore, the three segments of the Milun fault share the same rake angle bound of $[-90^\circ, 90^\circ]$. In addition, the middle segment of the Milun fault has the same dip angle with the south segment due to the short fault length of ca. 1.6 km. For the west-dipping fault, the bound is set as $[200^\circ, 220^\circ]$ for the strike angle, $[0^\circ, 90^\circ]$ for the dip angle, and $[-90^\circ, 90^\circ]$ for the rake angle based on the InSAR observations and field investigation. The depth of the west-dipping fault is also set as zero due to the interferometric decorrelation in the east of the west-dipping fault.

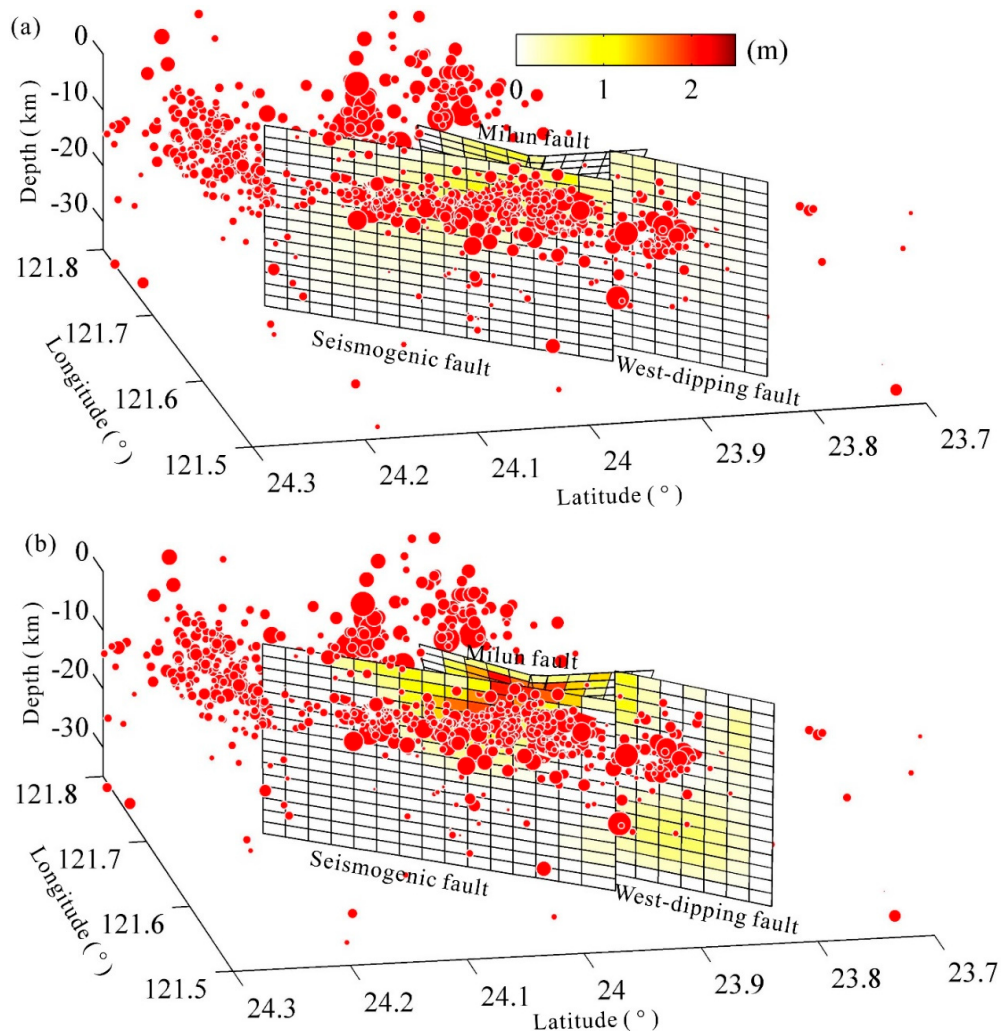


Figure 4. The faulting models respectively inferred by GPS and InSAR observations, and the red dots are the aftershocks of the 2018 Hualien earthquake. **(a)** The co-seismic faulting model inferred by GPS displacements with a peak slip of ca. 0.9 m. **(b)** The co-seismic and postseismic faulting model of the 2018 Hualien earthquake, in which the maximum accumulated slip magnitude is up to ca. 2.1 m.

The fault planes are firstly divided using the large size of $5\text{ km} \times 5\text{ km}$ along the strike and down-dip directions. Then, we carry out the best fitting fault geometry parameters searching in an elastic, homogeneous, and isotropic half-space based on the simulated annealing algorithm [24,25]. To get the global best fitting parameters, one hundred times above searching processes with random and individual starting values are performed. Finally, we re-divide the fault planes using the small size of $2\text{ km} \times 2\text{ km}$ along the strike and down-dip directions to obtain the fine slip distribution of the

2018 Hualien earthquake, the same process for studying the co-seismic slip deficit of the 2017 Mw 6.5 Ormoc earthquake [26].

3. Result

The estimated fault parameters and relative errors are shown in Table 2. The best fitting dip angle of the seismogenic fault is 89.4° , which is larger than the USGS solution of 73° . The estimated strike angle of the seismogenic fault is 201.7° , which is slightly less than 209° of the USGS solution. It is believed that the above differences should be due to the reason that the fault parameters are estimated by the different datasets of teleseismic waves for the USGS solution, but the near-fault InSAR observations for our study. In addition, Table 2 shows that both the Milun fault and the west-dipping fault have a high dip angle, which suggests a predominant strike-slip motion, showing a good consistency with the previous conclusion inferred from the distribution of the InSAR deformation fields.

Table 2. Estimated fault parameters of the 2018 Hualien earthquake.

Fault	Strike Angle ($^\circ$)	Dip Angle ($^\circ$)	Depth (km)	Rake Angle ($^\circ$)
Seismogenic fault	201.7 ± 3.7	89.4 ± 5.6	-17.4 ± 2.4	58.1 ± 8.7
Milun fault-south segment	0.1 ± 3.2	73.5 ± 4.2	0	44.9 ± 7.4
Milun fault-north segment	33.9 ± 5.4	71.8 ± 3.4	0	44.9 ± 7.4
West-dipping fault	206.3 ± 4.7	85.2 ± 2.7	0	11.8 ± 3.5

It should be noted again that we have not found a faulting model which simultaneously provides good fitness for both of the InSAR observations and GPS data. This suggests that the two datasets are incompatible in this study, and similar multiple-slip triggered phenomenon has also been found in the studies of the 2016 Mw 6.4 Meinong earthquake [7] and 2010 Mw 6.2 Jia-Shian earthquake [27] occurred in Southern Taiwan.

The used GPS displacements are solved based on the observations within four hours after the main quake of the 2018 Hualien earthquake. Therefore, the solved GPS displacements should be mainly contributed by the fault motion of the main quake. However, it can be found from Table 1 that the SAR images are captured by the satellites after 3–5 days after the main quake. In the interval between four hours and three days, the postseismic slip and large number of aftershocks could contribute to the surface deformation, which makes the InSAR deformation fields differ considerably from the GPS data.

Therefore, we hypothesize that the incompatibility between the two datasets should be due to the more surface deformation caused by the postseismic slip included in the InSAR observations, and we estimate the co-seismic faulting model based only on the GPS displacements. Figure 4a shows the estimated faulting model by the GPS data. It explains more than 98% of the GPS observations with model misfit of 0.9 cm (Figure 3), which suggests that the estimated faulting model can provide good fitness for the GPS displacements. The seismic moment calculated by the GPS-derived faulting model is 7.31×10^{18} Nm (Figure 5a), which is equivalent to a moment magnitude of Mw 6.52 and has a high consistency with the BATs and USGS solutions. In addition, we estimate the faulting model including the co-seismic and postseismic slip (Figures 4a and 5b) based on the InSAR observations. The estimated slip model explains 97.3% and 96.1% of the ALOS-2 ascending and descending data, and 95.8% and 93.4% of the Sentinel-1 ascending and descending data, respectively. Additionally, the model misfits are 0.9 cm of the ALOS-2 ascending data, 1.4 cm of the ALOS-2 descending data, 1.6 cm of the Sentinel-1 ascending data, and 0.9 cm of the Sentinel-1 descending data, respectively. Low model misfit suggests a high reliability of the estimated faulting model.

We forward calculate the predicted InSAR deformation (Figure 6a,c,e,h) based on the best fitting faulting model and the residuals between the predicted and observed data are shown (Figure 6b,d,f,h). It is obvious that both the predicted ALOS-2 and Sentinel-1 InSAR data have a good consistency with the observed results. The residual fringes in the east of the Milun fault should mainly result from

the lack of the modeling of some small shallow folds that have been triggered in the 2018 Hualien earthquake. In addition, some residual fringes can be found along the trace of the Milun fault, which could be attributed to the simple fault geometry model (only three plane segments) of the Milun fault. The residual fringes in the east of the west-dipping fault should predominantly result from the interferometric decorrelation. The other residual fringes should be mainly contributed by the atmospheric delay error and the phase unwrapping error.

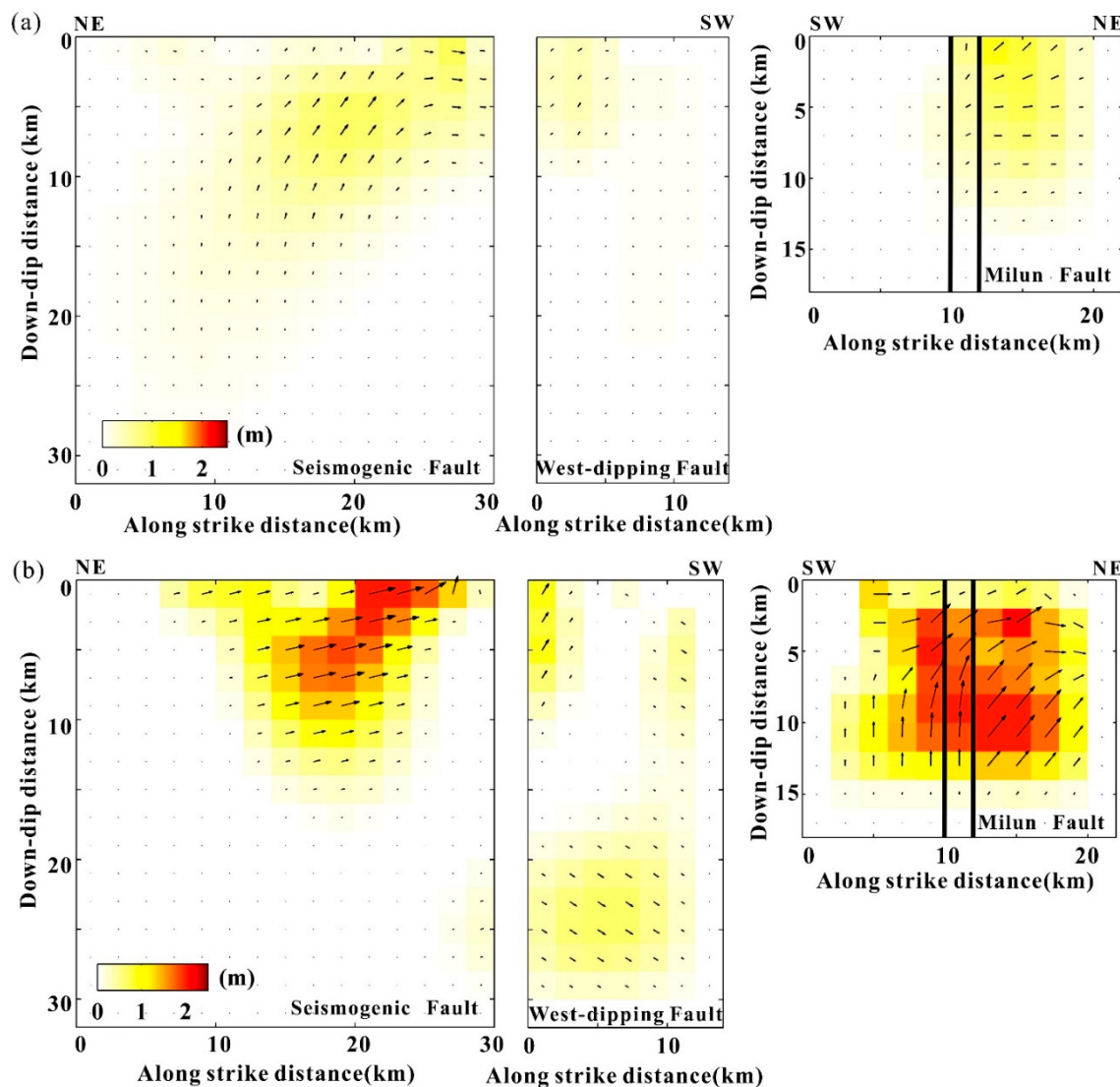


Figure 5. The planar fault slip distributions of the 2018 Mw 6.4 Hualien earthquake. The black lines denote the boundaries of the three segments of the Milun fault. (a) The estimated co-seismic fault slip distribution by the GPS data. (b) The estimated co-seismic and postseismic fault slip distribution by the four tracks InSAR observations.

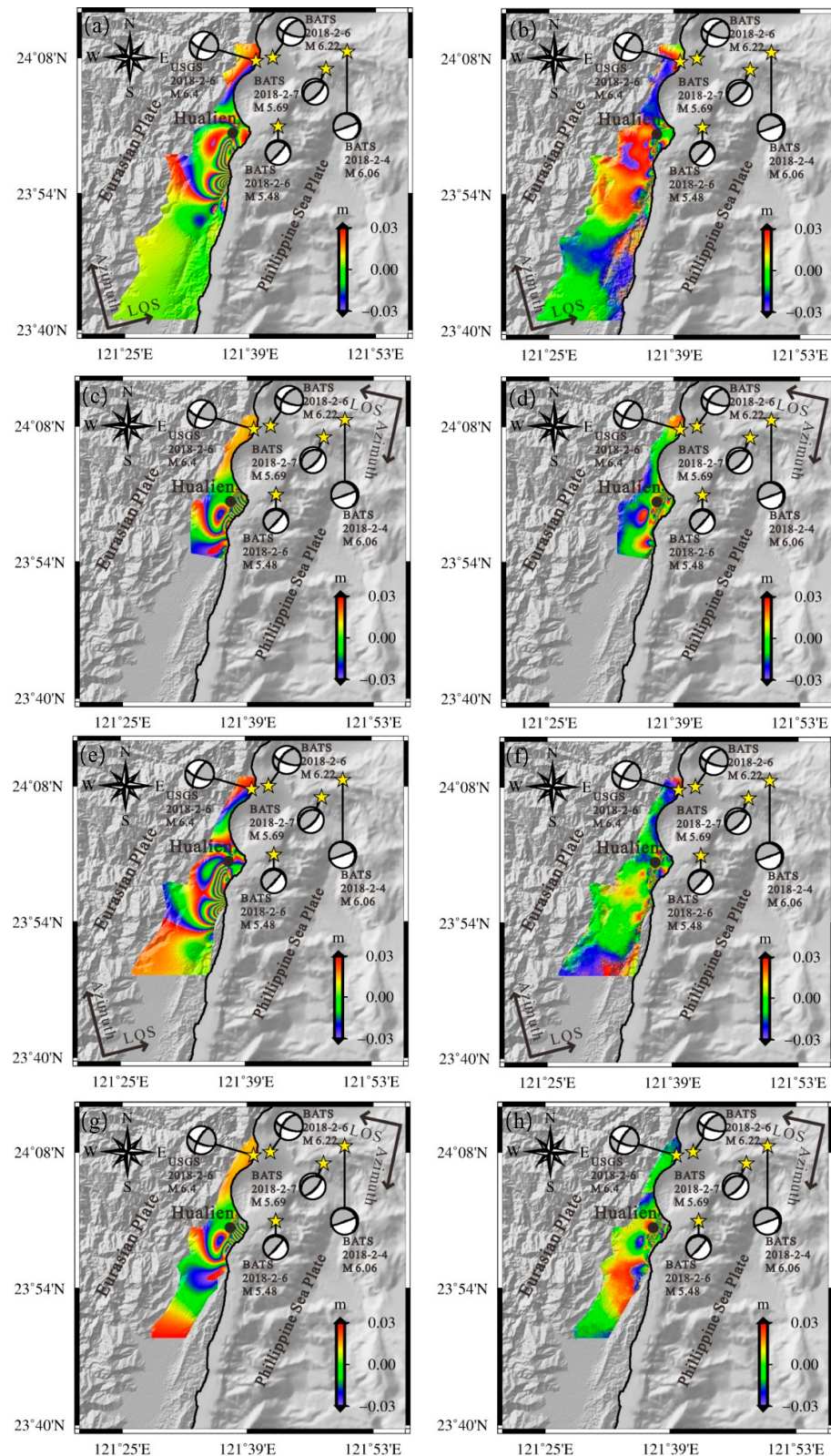


Figure 6. The predicted InSAR deformation using the faulting model shown in Figure 4b, and the residual between the observed (Figure 2) and predicted InSAR data. The predicted ALOS-2 ascending (a), ALOS-2 descending (c), Sentinel-1 ascending (e), and Sentinel-1 descending (d) InSAR deformation fields based on the preferred faulting model shown in Figure 4b. The residuals between the observed and predicted InSAR data of the ALOS-2 ascending (b), ALOS-2 descending (d), Sentinel-1 ascending (f), and Sentinel-1 descending (h).

4. Discussion

Figures 4 and 5 show that there are significant differences between the GPS-derived faulting model and the InSAR-derived result. First, the maximum slip of the InSAR-derived faulting model (Figure 5b) is ca. 2.1 m, which is significantly larger than ca. 0.9 m of the GPS-derived result (Figure 5a). Second, no slip is found in the south segment of the Milun fault from the GPS-derived faulting model. It suggests the south segment of the Milun fault does not rupture in the main quake and, thus, the derived slip (Figure 5b) from the InSAR observations is predominantly composed by the postseismic slip. In addition, both the seismogenic fault and west-dipping fault show that the InSAR-derived faulting model includes more postseismic slip than the GPS-derived result. It should also be noted that above result of the postseismic slip of the 2018 Hualien earthquake is only a preliminary result based on the co-seismic GPS data and the InSAR data, and more accurate determination of the postseismic slip needs further studies using the GPS and/or InSAR data observed at different times after the main quake.

Figure 5b shows that the co-seismic and postseismic slip concentrates at depths of 2.4–15 km on the seismogenic fault, which indicates that the rupture has not propagated to the ground surface. However, the maximum slip with magnitude of 2.1 m is located at the shallowest patch of the seismogenic fault. Here, we hypothesize the depth is 0–2.4 km of the shallow sedimentary section that cannot be transferred through by the fault rupture in Hualien area. Moreover, the slip on the seismogenic fault is controlled by the sinistral slip and slight reverse motion, and the significant slip concentrates at depths of 2.4–15 km and at along-strike distances of 10–27 km from the NE end of the seismogenic fault, which is consistent with the aftershock cluster. The seismic moment calculated by the estimated slip model of the seismogenic fault is 7.00×10^{18} Nm, which is equivalent to a moment magnitude of Mw 6.50.

The slip distribution in Figure 5b shows that the rupture on the Milun fault and the west-dipping fault has propagated to the ground surface, which should be partly responsible for the observed InSAR deformation in the seismic zone. The shallowest (within 0–2 km) fault slip of the Milun fault is controlled by the left-lateral strike-slip and slight reverse slip. Then, the rupture progressively transforms to a predominant reverse slip and slight left-lateral strike-slip at depths of 215 km. The calculated seismic moment of the Milun fault is 8.65×10^{18} Nm (equivalent to a moment magnitude of Mw 6.56), which is slightly larger than the result of the seismogenic fault. For the west-dipping fault, only slight slip is found in the NE end of the fault within depths of 0–8 km. The total seismic moment derived from the motion of the seismogenic fault, Milun fault and the west-dipping fault (near to the Lingding fault) is 1.57×10^{19} Nm and is equivalent to a moment magnitude of Mw 6.74, which is greater than the BATS and USGS solutions.

To evaluate the relationship between the seismogenic fault rupture and triggered fault motion, we calculate the Coulomb failure stress (CFS) change of the triggered faults using the co-seismic faulting model of the seismogenic fault (Figure 4a) derived from GPS displacements [28,29]. The receiver fault parameters of each fault patch including the strike angle, dip angle, and rake angle are set as the estimated values shown in Table 2 and Figure 4. The CFS change is calculated based on the Coulomb failure criterion with friction coefficient of 0.4, and the result is shown in the Figure 7a. The south segment of the Milun fault has a predominantly negative CFS change, which indicates the inhibition of the fault rupture. Then, Figure 5a shows that little slip is detected in the south segment of the Milun fault. The predominantly positive CFS change on the north segment of the Milun fault corresponds to that the significant fault slip is detected on it (Figure 5a). Slight CFS change in the west-dipping fault corresponds to the little slip on it (Figure 5a). Furthermore, we calculate the CFS change of the three faults (Figure 7b) after the main quake using the faulting model of all the faults (Figure 4a). However, none of remarkable positive relation is found between the postseismic slip (Figure 7b) and the positive CFS change. We hypothesize that the occurrence of the postseismic slip does not directly result from the CFS change.

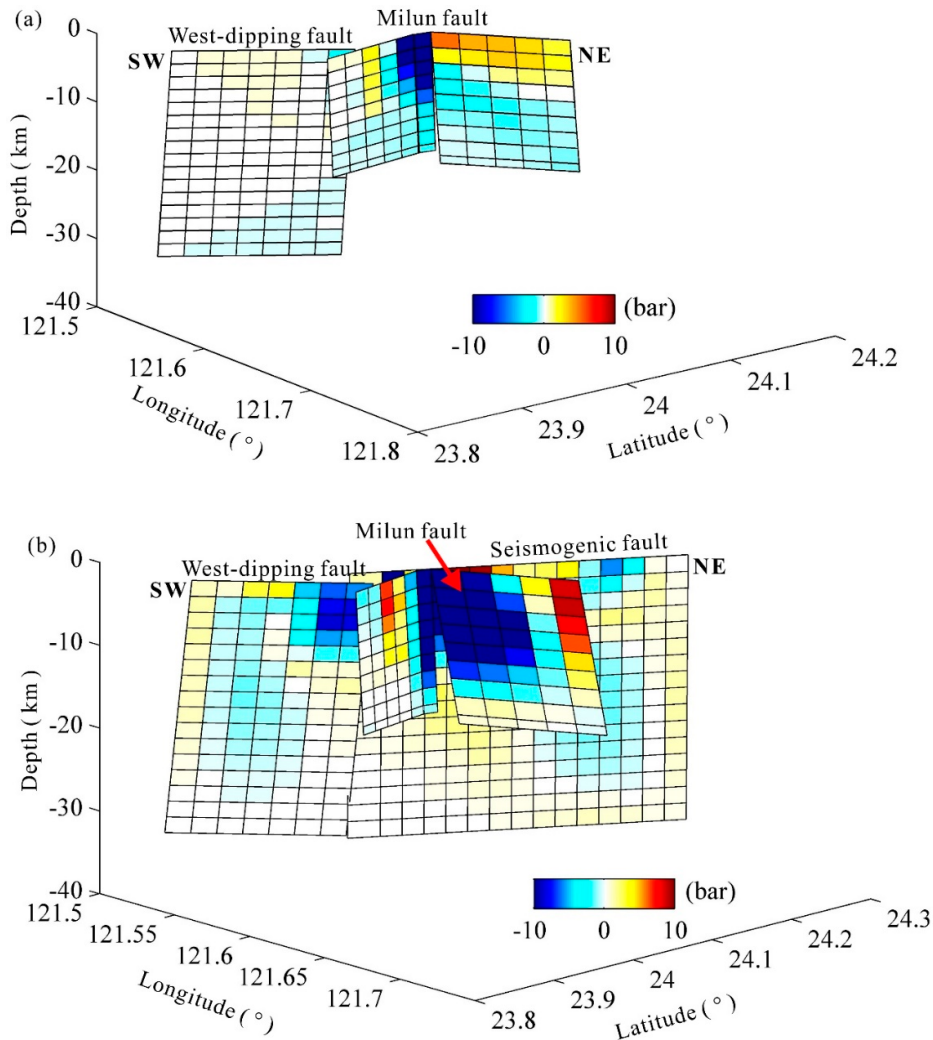


Figure 7. The Coulomb failure stress change on the faults. **(a)** The CFS change on the two triggered faults including the Milun and west-dipping faults calculated by the co-seismic faulting model of the seismogenic fault (Figure 4a). **(b)** The CFS change on all the faults calculated by the co-seismic faulting models shown in Figure 4a.

To access the risk of the future seismic hazard in the seismic zone after the 2018 Hualien earthquake, we calculate the CFS change at the depth of 10.0 km that is the average depth of the aftershocks, based on the inferred co-seismic and postseismic faulting model (Figure 4b) using different receiver parameters (see the caption of Figure 8 for the detailed parameters). Figure 8 shows the CFS change fields calculated by different receiver parameters, and it can be found from Figure 8e that the aftershocks have the highest consistence with the distribution of the positive CFS change when the receiver parameters are 135° for the rake angle, 0.1° for the strike angle, and 73.5° for the dip angle that are the same fault geometry as the south segment of the Milun fault, and more than ca. 70% aftershocks occurred in the significant positive CFS change zones of “A” in Figure 8e. The distinguished CFS change of “B” has an average positive CFS change of ca. 0.8 bar, but few aftershocks occur in this zone. Therefore, we hypothesize that there is a high possibility of the future seismic hazard in zone “B”. Figure 8e shows that some aftershocks occur in the negative CFS change zones, we hypothesize that it should result from the dynamic CFS and different CFS receiver parameters.

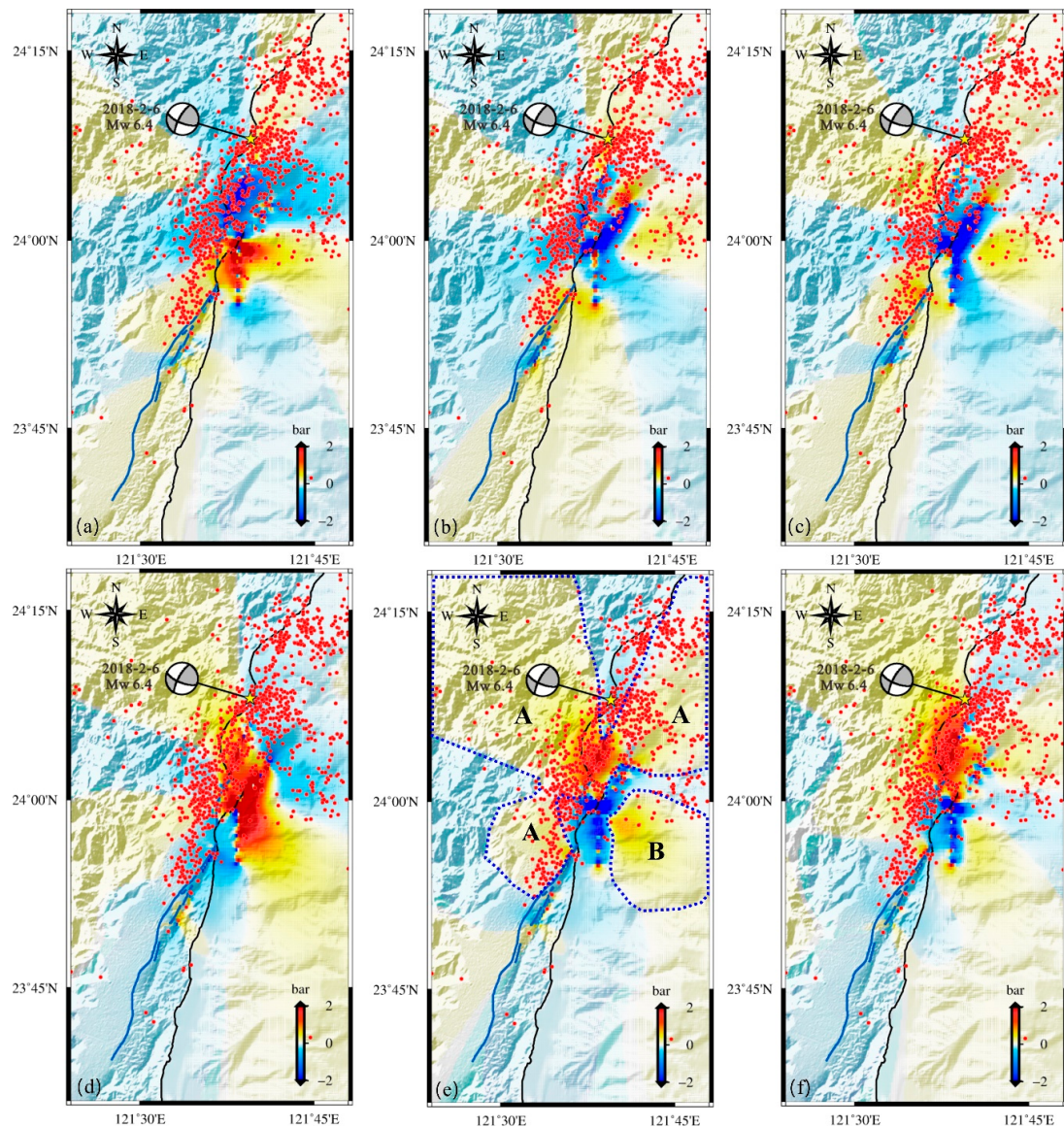


Figure 8. The Coulomb failure stress change at the depth of 10 km (the average depth of the aftershocks) with different receiver fault parameters. The red dots are the aftershocks of the 2018 Hualien earthquake, and the beach ball is the focal mechanism of the main shock of the 2018 Hualien event. The CFS change at the 10 km depth with receiver parameters of 201.7° for the strike angle, 89.4° for the dip angle, 45° (a) and 135° (d) for the rake angle. The CFS change at the 10 km depth with receiver parameters of 0.1° for the strike angle, 73.5° for the dip angle, and 45° (b) and 135° (e) for the rake angle. The CFS change at the 10 km depth with receiver parameters of 33.9° for the strike angle, 71.8° for the dip angle, and 45° (c) and 135° (f) for the rake angle. The blue dotted lines depict the significant positive CFS change areas.

5. Conclusions

In this study, the co-seismic and co-seismic and postseismic faulting models of the 2018 Mw 6.4 Hualien earthquake are estimated by the GPS and InSAR observations, respectively, and the GPS-derived co-seismic faulting model shows that three faults, including the seismogenic fault, the west-dipping fault dipping to the west, and the Milun fault dipping to the east, are responsible for the main quake. The InSAR-derived faulting model indicates that a great deal of postseismic slips occur on both the seismogenic and triggered faults, especially in the south segment of the Milun fault.

The calculated CFS change using the GPS-derived seismogenic faulting model shows that there is a predominant positive CFS change on the north segment of the Milun fault with significant co-seismic rupture, but a predominant negative CFS change in the un-ruptured south segment of the Milun fault. The relation between the CFS change and distribution of the aftershocks indicates that most of the aftershocks may have a similar fault geometry with the south segment of the Milun fault. Moreover, the significant positive CFS change zone of “B” may have a high risk of the future seismic hazard due to the few aftershocks that occurred in the area. Finally, this study suggests that the postseismic slip should be considered in the inversion of the faulting model, especially in studies where the used InSAR data are acquired one or more weeks after the main shock.

Author Contributions: Conceptualization, J.-C.H. and Y.-H.Y.; methodology, Y.-H.Y.; software, J.-J.Z., Y.-J.Z. and Q.X.; validation, J.-C.H. and Y.-H.Y.; formal analysis, H.T. and M.-C.T.; investigation, Q.C. and G.-X.L.; resources, M.-C.T.; data curation, Y.-H.Y., M.-C.T., Y.-J.Z., B.Y. and C.-Y.C.; writing—original draft preparation, Y.-H.Y.; writing—review and editing, J.-C.H.; visualization, J.-J.Z., J.-N.X., J.-Y.W. and Z.S.; supervision, Q.C. and G.-X.L.; project administration, Q.C.; funding acquisition, Q.C., G.-X.L. and J.-C.H.

Funding: This work is supported by the National Key R&D Program of China (2017YFB0502700), the Ministry of Science and Technology in Taiwan under the grant 106-2116-M-002-004, and the National Natural Science Foundation of China (41472255 and 51774250).

Acknowledgments: We are grateful to three anonymous reviewers and the editor for constructive comments that led us to significantly improve the manuscript. We benefitted from fruitful discussions with Wen-Shan Chen, Mong-Han Huang, Yo-Ho Chang, and Zhenhong Li. Appreciation is also owed to Hsiu-Fang Lee who helped us to prepare the figures. ALOS-2 SAR images were provided by the Japan Aerospace Exploration Agency (JAXA) under the ALOS-2 RA6 Project (PI No. 3255 and No. 3105), and the Sentinel-1A SAR images were provided by the European Space Agency (ESA). SRTM DEM data is the void-filled seamless SRTM data V4, available from the CGIAR-CSI SRTM 90 database: <http://srtm.cgiar.org/>. Figures were generated using the Generic Mapping Tools (GMT) software [30].

Conflicts of Interest: The authors declare no conflict of interest.

References

1. Lallemand, S.E.; Liu, C.S.; Font, Y. A tear fault boundary between the Taiwan orogen and the Ryukyu subduction zone. *Tectonophysics* **1997**, *274*, 171–190. [[CrossRef](#)]
2. Font, Y.; Liu, C.S.; Schnurle, P.; Lallemand, S. Constraints on backstop geometry of the southwest Ryukyu subduction based on reflection seismic data. *Tectonophysics* **2001**, *333*, 135–158. [[CrossRef](#)]
3. Lee, C.P.; Kim, K.H.; Huang, B.S.; Huang, W.G. Seismicity, active faults, stress patterns, and rupture processes in the Hualien region, Taiwan, investigated using the 1990 Hualien earthquake sequence. *Tectonophysics* **2011**, *511*, 27–37. [[CrossRef](#)]
4. Tsai, M.C.; Yu, S.B.; Shin, T.C.; Kuo, K.W.; Leu, P.L.; Chang, C.H.; Ho, M.Y. Velocity field derived from Taiwan continuous GPS array (2007–2013). *Terr. Atmos. Ocean. Sci.* **2015**, *26*, 527–556. [[CrossRef](#)]
5. Johnson, K.M.; Hsu, Y.J.; Segall, P.; Yu, S.B. Fault geometry and slip distribution of the 1999 Chi-Chi, Taiwan earthquake imaged from inversion of GPS data. *Geophys. Res. Lett.* **2001**, *28*, 2285–2288. [[CrossRef](#)]
6. Yu, S.B.; Kuo, L.C.; Hsu, Y.J.; Su, H.H.; Liu, C.C.; Hou, C.S.; Lee, J.F.; Lai, T.C.; Lui, C.C.; Liu, C.L.; et al. Preseismic deformation and co-seismic displacements associated with the 1999 Chi-Chi, Taiwan, earthquake. *Bull. Seismol. Soc. Am.* **2001**, *91*, 995–1012. [[CrossRef](#)]
7. Chen, K.H.; Toda, S.; Rau, R.J. A leaping, triggered sequence along a segmented fault: The 1951 ML 7.3 Hualien-Taitung earthquake sequence in eastern Taiwan. *J. Geophys. Res. Solid Earth* **2008**, *113*, B02304. [[CrossRef](#)]
8. Huang, M.H.; Tung, H.; Fielding, E.; Huang, H.H.; Liang, C.; Huang, C.; Hu, J.C. Multiple fault slip triggered above the 2016 Mw 6.4 MeiNong earthquake in Taiwan. *Geophys. Res. Lett.* **2016**, *43*, 7459–7467. [[CrossRef](#)]
9. Angelier, J.; Lee, J.C.; Chu, H.T.; Hu, J.C.; Lu, C.Y.; Chan, Y.C.; Lin, T.J.; Font, Y.; Deffontaines, B.; Tsai, Y.B. Le Séisme de Chichi (1999) et sa place dans l’orègene de Taiwan. (The Chichi earthquake, 1999, and its role in the Taiwan orogeny). *C. R. Acad. Sci. Paris Earth Planet. Sci.* **2001**, *333*, 5–21. [[CrossRef](#)]
10. Lin, K.C.; Hu, J.C.; Ching, K.E.; Angelier, J.; Rau, R.J.; Yu, S.B.; Tsai, C.H.; Shin, T.C.; Huang, M.H. GPS crustal deformation, strain rate and seismic activity after the 1999 Chi-Chi earthquake in Taiwan. *J. Geophys. Res.* **2010**, *115*, B07404. [[CrossRef](#)]

11. Jian, P.R.; Tseng, T.L.; Liang, W.T.; Huang, P.H. A New Automatic Full-Waveform Regional Moment Tensor Inversion Algorithm and Its Applications in the Taiwan Area. *Bull. Seismol. Soc. Am.* **2018**, *108*, 573–587. [[CrossRef](#)]
12. Bonilla, M.G. Summary of Quaternary faulting and elevation change in Taiwan. *Mem. Geol. Soc. China* **1977**, *2*, 43–55.
13. Yamaguchi, M.; Ota, Y. Tectonic interpretations of Holocene marine terraces, east coast of Coastal Range, Taiwan. *Quat. Int.* **2004**, *115*, 71–81. [[CrossRef](#)]
14. Hsu, T.L. Recent faulting in the Longitudinal Valley of eastern Taiwan. *Mem. Geol. Soc. China* **1962**, *1*, 95–102.
15. Chung, L.H.; Chen, Y.G.; Wu, Y.M.; Shyu, J.B.H.; Kuo, Y.T.; Lin, Y.N.N. Seismogenic faults along the major suture of the plate boundary deduced by dislocation modeling of co-seismic displacements of the 1951 M7.3 Hualien–Taitung earthquake sequence in eastern Taiwan. *Earth Planet. Sci. Lett.* **2008**, *269*, 416–426. [[CrossRef](#)]
16. Lee, Y.H.; Chen, G.T.; Rau, R.J.; Ching, K.E. Co-seismic displacement and tectonic implication of 1951 Longitudinal Valley earthquake sequence, eastern Taiwan. *J. Geophys. Res. Solid Earth* **2008**, *113*, B04305. [[CrossRef](#)]
17. Hamling, I.J.; Hreinsdóttir, S.; Clark, K.; Elliott, J.; Liang, C.; Fielding, E.; Litchfield, N.; Villamor, P.; Wallace, L.; Wright, T.J.; et al. Complex multifault rupture during the 2016 M w 7.8 Kaikōura earthquake, New Zealand. *Science* **2017**, *356*, eaam7194. [[CrossRef](#)] [[PubMed](#)]
18. Wegmüller, U.; Werner, C. Gamma SAR processor and interferometry software. In Proceedings of the 3rd ERS Symposium, Florence, Italy, 14–21 March 1997; pp. 1687–1692.
19. Farr, T.G.; Rosen, P.A.; Caro, E.; Crippen, R.; Duren, R.; Hensley, S.; Seal, D. The shuttle radar topography mission. *Rev. Geophys.* **2007**, *45*, 1–33. [[CrossRef](#)]
20. Yang, Y.H.; Chen, Q.; Xu, Q.; Zhang, Y.; Yong, Q.; Liu, G. Co-seismic surface deformation of the 2014 Napa earthquake mapped by Sentinel-1A SAR and accuracy assessment with COSMO-SkyMed and GPS data as cross validation. *Int. J. Digit. Earth* **2017**, *10*, 1197–1213. [[CrossRef](#)]
21. Rosen, P.A.; Gurrola, E.G.F.; Sacco, F.; Zebker, H. The InSAR scientific computing environment. In Proceedings of the 9th European Conference on Synthetic Aperture Radar, Nuremberg, Germany, 15 June 2012.
22. Cheloni, D.; De Novellis, V.; Albano, M.; Antonioli, A.; Anzidei, M.; Atzori, S.; Avallone, A.; Bignami, C.; Bonano, M.; Calcaterra, S.; et al. Geodetic model of the 2016 Central Italy earthquake sequence inferred from InSAR and GPS data. *Geophys. Res. Lett.* **2017**, *44*, 6778–6787. [[CrossRef](#)]
23. Welstead, S.T. *Fractal and Wavelet Image Compression Techniques*; SPIE Optical Engineering Press: Washington, DC, USA, 1999.
24. Okada, Y. Surface deformation due to shear and tensile faults in a half-space. *Bull. Seismol. Soc. Am.* **1985**, *75*, 1135–1154. [[CrossRef](#)]
25. Van Laarhoven, P.J.; Aarts, E.H. Simulated annealing. In *Simulated Annealing: Theory and Applications*; Springer: Dordrecht, The Netherlands, 1987; pp. 7–15.
26. Yang, Y.H.; Tsai, M.C.; Hu, J.C.; Aurelio, M.A.; Hashimoto, M.; Escudero, J.A.P.; Su, Z.; Chen, Q. Co-seismic slip deficit of the 2017 Mw 6.5 Ormoc Earthquake that occurred along a creeping segment and geothermal field of the Philippine Fault. *Geophys. Res. Lett.* **2018**, *45*, 2659–2668. [[CrossRef](#)]
27. Lin, K.C.; Delouis, B.; Hu, J.C.; Nocquet, J.M.; Mozziconacci, L. Reassessing the complexity of the rupture of the 2010 Jia-Shian Earthquake (Mw 6.2) in Southwestern Taiwan by inverting jointly teleseismic, strong-motion and CGPS data. *Tectonophysics* **2016**, *692*, 278–294. [[CrossRef](#)]
28. Chen, Q.; Yang, Y.; Luo, R.; Liu, G.; Zhang, K. Deep co-seismic slip of the 2008 Wenchuan earthquake inferred from joint inversion of fault stress changes and GPS surface displacements. *J. Geodyn.* **2015**, *87*, 1–12. [[CrossRef](#)]
29. Hanks, T.H. Earthquake stress-drops, ambient tectonic stresses, and the stresses that drive plates. *Pure Appl. Geophys.* **1977**, *115*, 441–458. [[CrossRef](#)]
30. Wessel, P.; Smith, W.H.F. New, improved version of Generic Mapping Tools released. *EOS Trans. Am. Geophys. Union* **1998**, *79*, 579. [[CrossRef](#)]

